

# Relationship between the nature of monovalent cations and charge recombination in metal halide perovskites

*Katelyn A. Dagnall<sup>1,†</sup>, Benjamin J. Foley<sup>1,†</sup>, Shelby A. Cuthriell<sup>1</sup>, Matthew R. Alpert<sup>1</sup>, Xiaoyu Deng<sup>1</sup>, Alexander Z. Chen<sup>1</sup>, Zeming Sun<sup>2</sup>, Mool C. Gupta<sup>2</sup>, Kai Xiao<sup>3</sup>, Seung-Hun Lee<sup>4</sup>, Ying-Zhong Ma<sup>5</sup> and Joshua J. Choi<sup>1,\*</sup>*

<sup>1</sup> Department of Chemical Engineering, University of Virginia, Charlottesville, Virginia 22904, USA

<sup>2</sup> Department of Electrical and Computer Engineering, University of Virginia, Charlottesville, Virginia 22904, USA

<sup>3</sup> Center for Nanophase Materials Sciences, Oak Ridge National Laboratory, Oak Ridge, Tennessee 37831, USA

<sup>4</sup> Department of Physics, University of Virginia, Charlottesville, Virginia 22904, USA

<sup>5</sup> Chemical Sciences Division, Oak Ridge National Laboratory, Oak Ridge, Tennessee 37831, USA

<sup>†</sup>These authors contributed equally to this work

\*Corresponding author (email: jjc6z@virginia.edu)

## Abstract

We report charge recombination rates in lead iodide perovskites with alloys of formamidinium (FA) and methylammonium (MA) cations,  $\text{FA}_x\text{MA}_{1-x}\text{PbI}_3$ ,  $0 \leq x \leq 0.9$ , prepared through ion exchange with minimal differences in morphology and charge trap density. Our results show that the trap-mediated recombination rate increases over two orders of magnitude with decreasing MA content. These results are consistent with a proposed mechanism that MA molecules are more effective in screening charged defects. In contrast, band-to-band charge recombination rates are minimized at an intermediate alloy composition. These findings reveal that the monovalent cations impact recombination processes through different mechanisms.

Metal halide perovskites (MHPs) with structure  $ABX_3$ , in which A is a monovalent cation (methylammonium:  $MA^+$ , formamidinium:  $FA^+$ , cesium:  $Cs^+$ ), B is a divalent metal ( $Pb^{2+}$ ), and X is a halide ( $I^-$ ,  $Cl^-$ ,  $Br^-$ )<sup>1</sup>, have shown significant promise as optoelectronic materials for their high device performance and low-cost manufacturing process. While MHP solar cells and light-emitting diodes (LEDs) have undergone rapid increases in performance over the past decade, there are still gaps in the fundamental knowledge of these materials, particularly in the role of the A-site monovalent cation, that may be limiting further improvement and application.<sup>2-5</sup>

The two characteristics that are largely responsible for the high performance of MHPs are their extremely long charge carrier lifetimes with low rates of charge recombination<sup>6</sup>, and their tolerance of trap states, even in the presence of a high density of defects in polycrystalline MHP films<sup>7</sup>. Mechanisms proposed to explain these characteristics include polaron formation<sup>4,8-10</sup>, and the Rashba effect<sup>11,12</sup>, with several reports presenting evidence for the existence of each mechanism<sup>13-15</sup>. The role of the monovalent cation in enhancing these mechanisms, extending charge carrier lifetimes, and promoting defect tolerance, is currently under intense debate. The monovalent cation does not directly contribute to the band-edge electronic states<sup>16</sup>, but the cation size, dipole, and free rotation can all influence and distort the lead halide network which, ultimately, can alter its optoelectronic properties.

A recent study by Tan *et al.* determined that the inclusion of the strong dipolar  $MA^+$  cation to a sample containing  $FA^+$  and  $Cs^+$  cations lengthened the overall charge carrier lifetime, and reduced the density of deep charge trap states<sup>7</sup>. The authors attributed these effects to the  $MA^+$  dipole reorienting in response to local electric fields created by charged defects, thereby reducing the defect charge and capture cross section experienced by free carriers. This study inspires the questions: 1) Is this an intrinsic effect of the  $MA^+$  cation itself, or is it an alloy effect of the multiple cations working together? High performance MHP compositions are almost exclusively mixed cations, and the origin of this trend is not well understood. And, 2) could the cation have an effect on the bimolecular (band-to-band) recombination rate constant, in addition to the monomolecular (trap-mediated) recombination rate constant? To address these questions, a careful comparison must be made of the cations, in a compositional range that allows for not only the study of the effect of each cation independently, but also the effect of alloying multiple cations together. However, previous works studying a range of MHP cation compositions have encountered variations in sample morphology with potential changes in trap state density, which complicate direct comparison of the cations<sup>18,19</sup>.

In this work, we present a systematic study of  $FA_xMA_{1-x}PbI_3$  MHP alloys with MA:FA ratio,  $x$ , ranging from 0 to 0.9 with comparable morphologies and densities of charge trap states to determine trends in monomolecular recombination rate constant through time-resolved photoluminescence (TRPL), and in bimolecular recombination rate constant through femtosecond transient absorption (TA) measurements. A cation exchange procedure was employed to achieve consistent morphology, grain size, structure, and trap state density throughout the range of seven cation alloy compositions from  $MAPbI_3$  to  $FA_{0.9}MA_{0.1}PbI_3$ . Consistent trap state densities were confirmed through trap-filled limited voltage ( $V_{TFL}$ ) measurements. Our results show that the monomolecular recombination rate constants exponentially increase by two orders of magnitude

as the FA content is increased despite the similar charge trap densities, indicating that the nature of the monovalent cation plays a critical role in trap mediated recombination. Moreover, our results further show reduced bimolecular recombination upon alloying of the monovalent cations; while the MA and FA rich alloys have similar bimolecular recombination rate constants, there is a minimum at intermediate alloyed compositions. These results suggest that the monomolecular and bimolecular recombination rates can be separately tailored for different device applications by engineering the monovalent cation composition.

### FA<sub>x</sub>MA<sub>1-x</sub>PbI<sub>3</sub> thin film cation exchange and characterization

Alloys of FA and MA were chosen as our model system, as these cations have varying shape and strength of dipole, but similar enough molecular sizes in which, unlike Cs alloy systems, a full and stable range of lead halide perovskite alloys can be prepared under identical conditions. Standard MHP alloy thin film fabrication methods, such as spin-coating and thermal annealing of precursor solutions of varying alloy composition, result in significantly different crystallization processes and film morphologies<sup>19</sup>. For this reason, cation exchange process was chosen as the alloy fabrication method, in which seven MAPbI<sub>3</sub> films were synthesized through the highly reproducible, two-step interdiffusion method, and each sample was submerged in one of seven solutions of different FA:MA ratio<sup>20,21</sup>. The aim was to produce seven FA<sub>x</sub>MA<sub>1-x</sub>PbI<sub>3</sub> films of varying FA:MA ratio with the morphology and grains of the original MAPbI<sub>3</sub> films preserved.

Characterization of the FA<sub>x</sub>MA<sub>1-x</sub>PbI<sub>3</sub> thin films dissolved in deuterated dimethyl sulfoxide (DMSO) conducted by solution phase proton nuclear magnetic resonance (<sup>1</sup>H NMR) determined that a range of cation compositions of  $0 \leq x \leq 0.9$  was achieved, and that the compositions of the thin films were close to that of the cation exchange solutions (Fig. 1a). X-ray diffraction (XRD) results show a monotonic increase in lattice size with increasing mole fraction of the FA cation based on the shift of the (110) peak due to the larger size of the FA cation compared to MA, suggesting homogeneous mixture of FA and MA. The full width half maximum of the (110) peak is similar for all cation alloy compositions, indicating similar crystallinity (Fig. 1b). The peaks of photoluminescence (PL) emission spectra also showed a monotonic redshift (Fig. 1c) with increasing FA content, further confirming homogeneous mixing of the FA and MA cations.

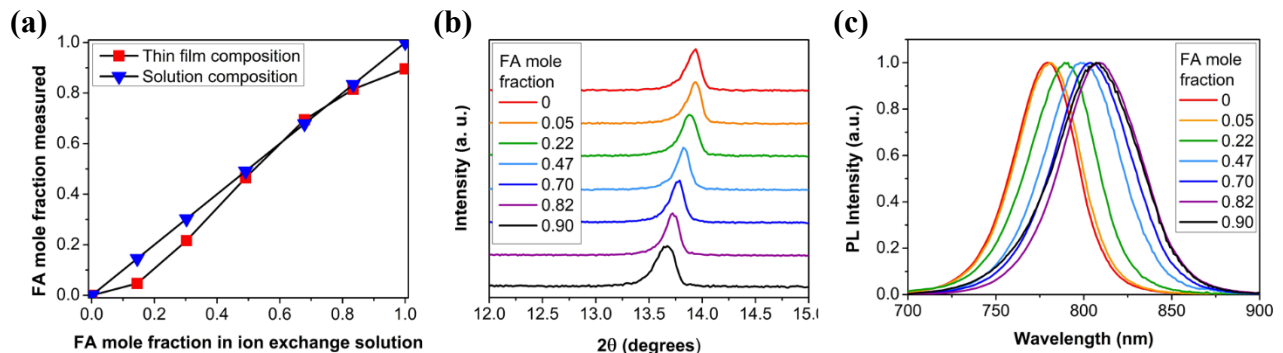


**Figure 1.** (a) Composition of the cation exchange solution and resultant thin films characterized by  $^1\text{H}$  NMR, (b) tetragonal (110) or cubic (100) X-ray diffraction peaks, and (c) photoluminescence emission spectra of seven  $\text{FA}_x\text{MA}_{1-x}\text{PbI}_3$  films with different FA mole fraction  $x$ .

Upon examination with scanning electron microscopy (SEM), the grain sizes of all  $\text{FA}_x\text{MA}_{1-x}\text{PbI}_3$  thin films were found to be similar (Fig. 2a). Pinholes are apparent in the morphology, but are consistent in size and form throughout the cation range. To further ensure that any differences in charge traps due to different morphology would not impact the monomolecular recombination rate, trap state densities of all samples were determined through measuring trap-filled limited voltage ( $V_{\text{TFL}}$ )<sup>22,23</sup>. An example of the  $V_{\text{TFL}}$  measurement results obtained from the  $\text{FA}_{0.7}\text{MA}_{0.3}\text{PbI}_3$  sample can be found in Fig. 2b.  $V_{\text{TFL}}$  results from all alloys are included in the Supporting Information. The intersection of the two is the  $V_{\text{TFL}}$ , which can be used in Equation 1 to determine trap state density ( $N_t$ ).

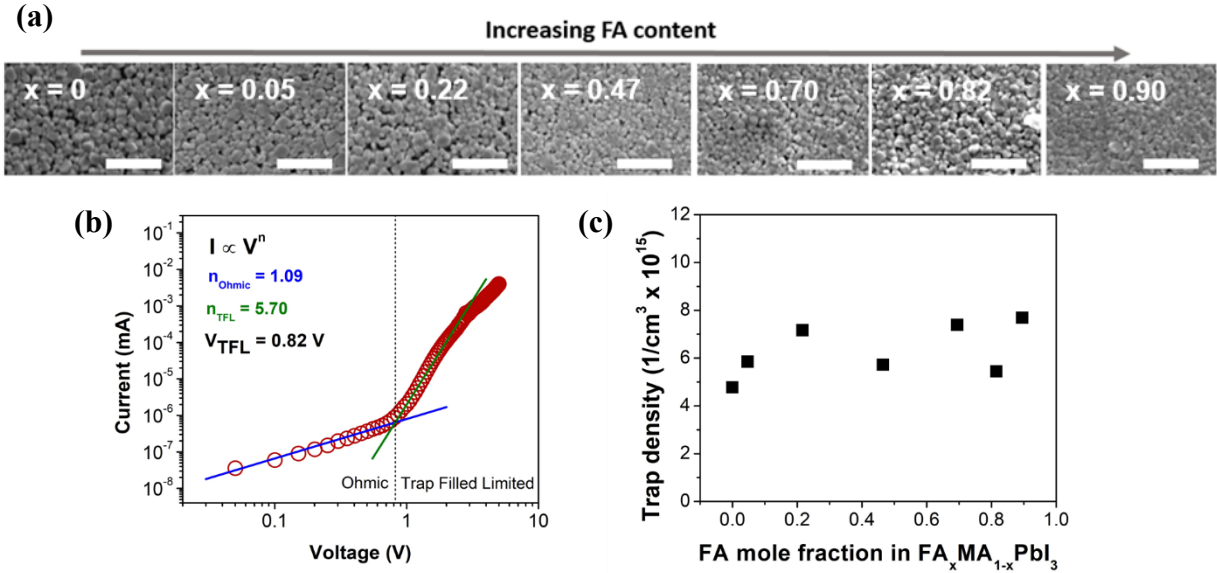


**Figure 2.** (a) SEM images of  $\text{FA}_x\text{MA}_{1-x}\text{PbI}_3$  thin films in which  $x$  ranges from 0 to 0.9. Scale bars are  $2 \mu\text{m}$ . (b) An example current-voltage curve for a  $\text{FA}_{0.7}\text{MA}_{0.3}\text{PbI}_3$  device, with the  $V_{\text{TFL}}$  at the intersection of the blue and green lines. (c) The trap site densities ( $N_t$ ) determined from  $V_{\text{TFL}}$ .

$$N_t = \frac{2\varepsilon_0\varepsilon V_{\text{TFL}}}{eL^2}n^2 \quad (\text{Equation 1})$$

In this equation,  $\varepsilon_0$  is the vacuum permittivity,  $\varepsilon$  is the relative dielectric constant of the alloy,  $e$  is the electron charge, and  $L$  is the thickness of the film<sup>24</sup>. Trap density as a function of FA mole fraction,  $x$ , is plotted in Fig. 2c, and shows no significant change across the entire range of  $\text{FA}_x\text{MA}_{1-x}\text{PbI}_3$  alloy samples. In summary, of the combination of XRD, PL, SEM, and  $V_{\text{TFL}}$  results confirms that our  $\text{FA}_x\text{MA}_{1-x}\text{PbI}_3$  samples have negligible difference in extrinsic factors, such as trap density, grain size, and phase separation, ultimately enabling us to probe the intrinsic

relationship between the monovalent cation composition and the charge carrier recombination dynamics.

### Monomolecular (trap-mediated) recombination rate

To probe the monomolecular recombination rate in the  $\text{FA}_x\text{MA}_{1-x}\text{PbI}_3$  thin films, we performed TRPL measurements using a 500 nm pulsed laser at a fluence of  $0.05 \mu\text{W}/\text{cm}^2$ , corresponding to  $\sim 10^{15}$  photoexcited carriers/ $\text{cm}^3$  (see Experimental Section for further details). At this low carrier density, charge recombination is dominated by trap-mediated processes, and the first order decay curves shown in Fig. 3a are indicative of dominant monomolecular recombination<sup>25–27</sup>. As  $x$  in  $\text{FA}_x\text{MA}_{1-x}\text{PbI}_3$  increases, there is a clear trend of faster charge carrier decay rates. The monomolecular recombination rate constant,  $k_m$ , was determined from fitting the TRPL data to the first order decay process described in Equation 2.

$$\frac{dn}{dt} = -k_m n = -k_t N_t n n^2 \quad (\text{Equation 2})$$

Our results show that  $k_m$  increases monotonically by two orders of magnitude as the FA mole fraction increases from  $\text{MAPbI}_3$  to  $\text{FA}_{0.9}\text{MA}_{0.1}\text{PbI}_3$  (Fig. 3b). The extrinsic influence of trap state density can be eliminated using the  $N_t$  measured with  $V_{\text{TFL}}$  to determine the rate constant at which charge carriers recombine per charge trap ( $k_t$ ), which also shows an increase by two orders of magnitude over the range from  $\text{MAPbI}_3$  to  $\text{FA}_{0.9}\text{MA}_{0.1}\text{PbI}_3$  (Fig. 3c).

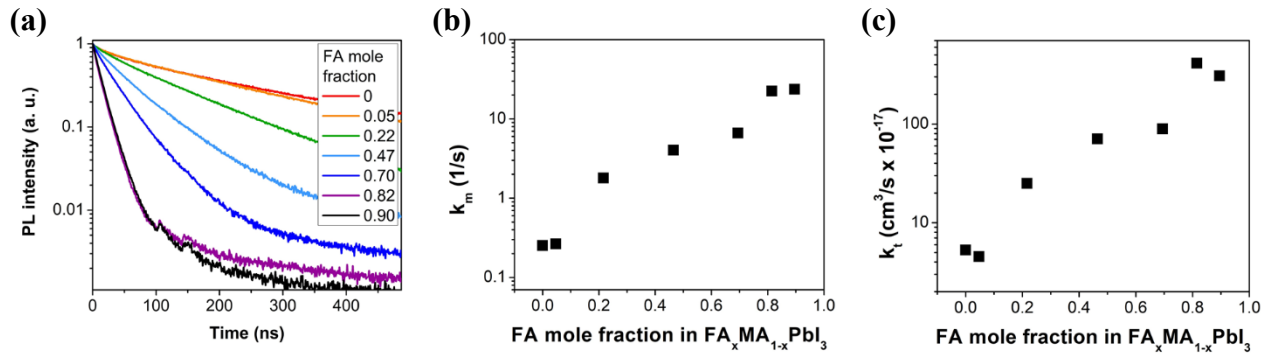


**Figure 3.** (a) Time resolved photoluminescence curves. (b) Monomolecular recombination rate constant ( $k_m$ ) and (c) rate constant at which charge carriers recombine per charge trap ( $k_t$ ) at different FA mole fraction.

There are several mechanisms proposed in the literature to explain the trapping of free carriers and the subsequent emptying of those traps. These range from Shockley-Read-Hall recombination<sup>28</sup> to mechanisms proposed by Stranks *et al.*<sup>29</sup> and others<sup>30–32</sup>. Given that the two orders of magnitude change in trap-mediated recombination rate constant is independent of trap density, the change must have resulted from differences in the parameters which describe how the charge carriers interact with traps. Our results support the proposed mechanism that the polar organic cations may play a role in screening charge carriers from trap-mediated recombination, potentially through the formation of polarons<sup>4,13,33</sup>. Another possibility is that the charged defects which form the trap

sites are either statically or dynamically screened by the polar cations, shifting the trap states to shallower energy levels, and consequently making them less active as recombination centers<sup>34</sup>. The screening of a charged species by the polar organic cation is key to both mechanisms, and the greater effectiveness in reducing trap-mediated recombination by the strong dipolar MA cation compared to the weaker dipolar FA cation<sup>2</sup>, is experimental evidence for the occurrence of this polar organic cation induced screening. Our result further confirms that the nature of the monovalent cation has a significant role in the “defect-tolerance” of metal halide perovskites, and enables their high performance in polycrystalline thin films.

### Bimolecular (band-to-band) recombination rate

Transient absorption (TA) decay kinetics were collected using 500 nm pump and 780 nm probe wavelengths at four different pump intensities between 5 and 65  $\mu\text{W}/\text{cm}^2$ , corresponding to  $1.9 \times 10^{17}$  to  $2.6 \times 10^{18}$  photoexcited carriers per  $\text{cm}^3$ . The bimolecular recombination rate constant  $k_b$  was determined using a global fitting algorithm based on Equation 3 for all TA decay curves measured at different pump intensities.

$$\frac{dn}{dt} = D \frac{d^2n}{dx^2} - k_m n - k_b n^2 \quad (\text{Equation 3})$$

where  $n$  is the photoexcited carrier concentration and  $D$  is the carrier diffusion coefficient. Given that the film thickness is approximately 300 nm and the majority of excitation light is absorbed in the first 50 nm, it was necessary to include the diffusion term as shown before<sup>34</sup>. No evidence of the third order Auger recombination was found at the pump intensities used in the measurements, and therefore it was not included in the model. As the probe wavelength is within the PL spectra shown in Figure 1c, the dominant transient absorption signal measured at the selected probe wavelength was found to be ground state photobleaching in combination with stimulated emission. Because the photoinduced absorbance change in a transient absorption measurement can be written as  $\Delta OD = n(-\sigma_{PB} - \sigma_{SE} + \sigma_{ESA})$ , where the first two terms describe the cross-sections of ground state bleaching and stimulated emission, respectively, and the last term is cross-section of photo-induced absorption, the observed change in absorbance ( $\Delta OD$ ) is directly proportional to the excited carrier concentration<sup>35-37</sup>. The TA decay curves collected at  $1.3 \times 10^{18}$  carriers/ $\text{cm}^3$  for all samples with different FA mole fractions along with their corresponding  $k_b$  values extracted from the global fit are shown in Figure 4.

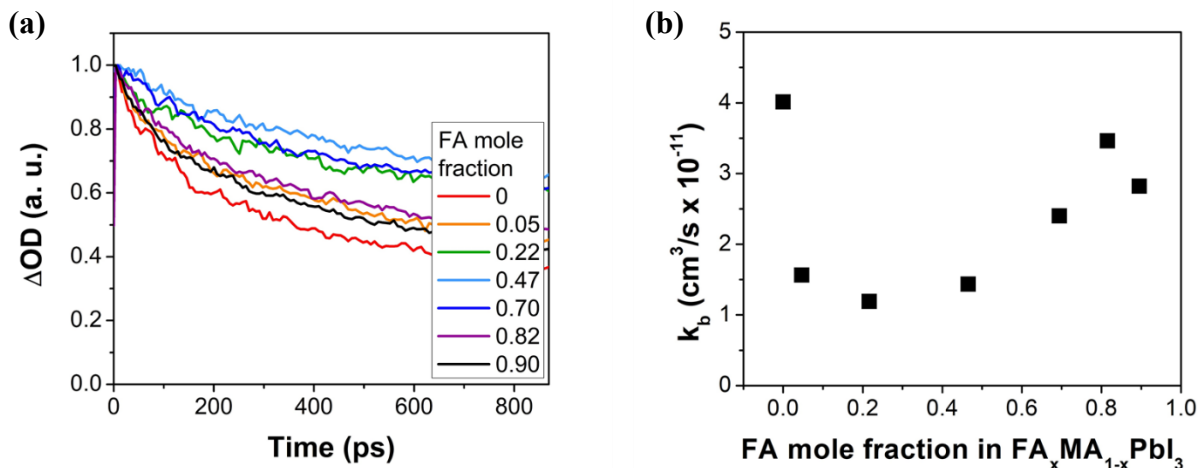


**Figure 4.** (a) Transient absorption decay curves collected for seven  $FA_xMA_{1-x}PbI_3$  films with different FA mole fraction  $x$  at an excitation density of  $1.3 \times 10^{18}$  carriers/cm<sup>3</sup>. (b) The bimolecular recombination rate constant ( $k_b$ ) as a function of FA mole fraction.

Our results in Fig. 4b show that there is no significant difference in the bimolecular recombination rate constants between MAPbI<sub>3</sub> and FA rich compositions. This lack of difference in the bimolecular recombination in lead iodide perovskites with different monovalent cations is consistent with work done by Dastidar et al.<sup>38</sup>, on CsPbI<sub>3</sub> and MAPbI<sub>3</sub> systems. However, interestingly, our results show a minimum in  $k_b$  at around FA mole fraction of 0.2 which suggests that alloying the monovalent site cations has a significant impact on bimolecular recombination rate. The bow shape of  $k_b$  versus FA mole fraction resembles the entropy of mixing, and it is possible that the increased disorder in structure or dynamics impact polaron formation or charge screening. Other possibilities involve nanoscale distortions to the crystal lattice, or localized electric fields, resulting in the electron and hole being separated in real space<sup>5</sup>, or momentum space<sup>11,39</sup>. These effects can be enhanced by the increase in entropy or structural disorder created by the alloyed system which translates into enhanced formation of local domains or a wider distribution of energetic states.

The typical conclusion of previous studies is that monovalent cation composition influences the overall trap site density, as opposed to changing the interaction between the carriers and trap sites.<sup>40,41</sup> It is worth noting that most of these studies used more convoluted materials systems and thin film processing methods compared to our study, causing complications in distinguishing intrinsic materials properties from extrinsic factors such as crystal quality. Due to possibly similar reasons, previous studies focusing on the  $FA_xMA_{1-x}PbI_3$  system report a wide range of conclusions as to how the monovalent cation impacts monomolecular recombination.<sup>42-46</sup> As FA rich compositions typically result in thin films with larger grain sizes when prepared through typical spin-coating and thermal annealing methods, this likely results in lower overall trap site density and masks the trend of monomolecular recombination increasing with FA content.

Our finding that inclusion of FA results in higher monomolecular recombination rate than MA seems contrary to the fact that many of the most efficient solar cells use FA rich compositions. However, a recent study by Sargent and co-workers<sup>7</sup> on the trap site density, trap site energy levels, and TRPL curves in  $Cs_{0.2}FA_{0.8}Pb(I_{0.75}Br_{0.25})_3$  and  $Cs_{0.05}MA_{0.15}FA_{0.8}Pb(I_{0.75}Br_{0.25})_3$  systems convincingly show that the dipolar MA cations screen the trap sites in ways the FA and Cs cations cannot. Ultimately, they concluded that addition of MA results in the trap states shifting to shallower energy levels which ultimately lowers the monomolecular recombination rate. Our study employed an approach that enabled a direct probe of the impact of monovalent cation compositions on charge trapping rate without significantly changing the charge trap densities as a function of monovalent cation compositions. The consistent and drastic change in charge trapping rate per trap site as a function of monovalent cation composition that was found in our work highlights the importance of rationally selecting monovalent cation composition to improve the MHP device performance.

Moreover, our findings that the monomolecular and bimolecular recombination rates exhibit different trends with monovalent cation composition reveals another important characteristic of

MHPs. There is a consensus that both the monomolecular and bimolecular recombination rates in MHP are unusually low considering the amounts of defects and traps present in them.<sup>6,9,25</sup> However, whether or not the same mechanisms are responsible for slowing down both recombination pathways is still unclear. The theories regarding the role of the monovalent cation in slow charge recombination processes involve reorientation of the dipole to screen charge carriers<sup>9</sup> or trap sites,<sup>7</sup> or enhancement of a Rashba effect by the polar cations.<sup>11</sup> Our results favor either of the following two possibilities: (1) the monovalent cations influence the monomolecular and bimolecular recombination processes through different mechanisms. It is possible that that dynamic screening, for example in polaron formation, is responsible for suppressed bimolecular recombination while static screening of charged defects is more dominant in suppressing monomolecular recombination. (2) Majority of monomolecular and bimolecular recombination processes occur at different locations such as surface versus bulk<sup>9</sup> while the influence of the monovalent cation, for example due to reorientation of the dipole, are different depending on the location. At the surface, dangling bonds or charged defects may create strong local electric fields which are not present in the bulk crystals. It is conceivable that the different local electrostatic environment of the surface can significantly alter the geometry and timescale with which the polar cations reorient compared to more freely rotating polar cations in the bulk, ultimately resulting in different interactions with free charge carriers.

In summary, our work shows that the nature of the monovalent cation has drastically different impact on monomolecular and bimolecular recombination processes. Changing the monovalent cation composition can alter the intrinsic monomolecular recombination rate by two orders of magnitude. As for bimolecular recombination rate, MHPs with alloyed monovalent cations can have lower bimolecular recombination than pure phases. Taken together, these results show that the nature of the monovalent cations plays a critical role in charge carrier recombination processes with different influences in mechanisms that dominate the bimolecular and monomolecular recombination rates. The implications of our findings on the technological applications of our findings are that monomolecular and bimolecular recombination processes can be optimized separately, perhaps even independently. Selecting a MHP composition which minimizes both monomolecular and bimolecular recombination rates is desirable in applications such as solar cells, where slow recombination in both pathways is ideal. On the other hand, light-emitting diode applications will benefit from slow trap-mediated monomolecular recombination but fast radiative bimolecular recombination. Therefore, rational selection of monovalent cation compositions tailored for specific applications will be a key to achieve high device performance.

## **Experimental Methods**

**Materials.** All materials used in this work were purchased from Sigma-Aldrich, with the exception of the following: pre-patterned indium tin oxide (ITO,  $15 \Omega \text{ cm}^{-2}$ ) from Kintec, lead iodide ( $\text{PbI}_2$ , 99.99%) from TCI Chemicals, methylammonium iodide ( $\text{CH}_3\text{NH}_3\text{I}$ ) and formamidinium iodide ( $\text{CH}_3(\text{NH}_3)_2\text{I}$ ) from Dyesol Inc.

**Thin film fabrication & cation exchange.** To prepare the perovskite thin films, 1 inch<sup>2</sup> glass microscope slides were cleaned in series under sonication with: detergent, de-ionized water and 2-

propanol. The slides were rinsed with acetone and 2-propanol before being air dried and cleaned with a Jelight ultra-violet ozone cleaner.

To improve perovskite adhesion during the cation exchange procedure, the glass slides were coated with a layer of  $\text{Al}_2\text{O}_3$  by spincoating 60  $\mu\text{L}$  of 1 mg/mL aluminum acetylacetonate in ethanol at 2000 rpm and annealing at 500  $^\circ\text{C}$  for 10 minutes.

The  $\text{CH}_3\text{NH}_3\text{PbI}_3$  perovskite layers were synthesized using a modified version of the two-step interdiffusion method<sup>54</sup> in a nitrogen filled glovebox. 1M  $\text{PbI}_2$  in DMSO/DMF was spincoated on the glass/ $\text{Al}_2\text{O}_3$  slides at 2000 rpm for 60 seconds, immediately after which 50 mg/mL  $\text{CH}_3\text{NH}_3\text{I}$  in 2-propanol was spincoated at 2000 rpm for 60 seconds to allow the  $\text{CH}_3\text{NH}_3\text{I}$  to diffuse into the  $\text{PbI}_2$  film. The slides were then annealed at 110  $^\circ\text{C}$  for 12 minutes.

The cation exchange solutions were prepared by dissolving the target molar ratios of  $\text{CH}_3\text{NH}_3\text{I}$  and  $\text{CH}_3(\text{NH}_3)_2\text{I}$  in anhydrous butanol at a concentration of 0.01 M. The  $\text{CH}_3\text{NH}_3\text{PbI}_3$  films were soaked in the cation exchange solutions for 15 hours to allow time for the cation exchange to reach equilibrium. After soaking, the films were removed, rinsed with an excess of anhydrous butanol to remove surface cations, dried with nitrogen and annealed at 100  $^\circ\text{C}$  for 10 minutes.

For photoluminescence and transient absorption measurements, the films were encapsulated with a coverslip sealed with optical cement epoxy, and ultra-violet light cured for 10 minutes.

**$^1\text{H}$ -Nuclear magnetic resonance spectroscopy measurements.** The compositions of the cation exchanged films were characterized using  $^1\text{H}$ -NMR with a Varian Inova 500 spectrometer. The cation exchanged films were prepared for  $^1\text{H}$ -NMR through digestion in 1 mL of deuterated DMSO, which was repeated for 8 films of each cation composition to ensure high enough concentration in solution. The  $^1\text{H}$ -NMR data were analyzed by integrating the characteristic  $\text{CH}_3\text{NH}_3^+$  peak at 2.35 ppm, and the characteristic  $\text{CH}_3(\text{NH}_3)_2^+$  peak at 7.85 ppm.

**Additional characterization.** The cation exchanged film morphologies were characterized using a FEI Quanta 650 Scanning Electron Microscope. The crystal structures of the films were characterized with X-ray diffraction using a PANalytical X'Pert Pro Multi-Purpose Diffractometer at 40 kV and 40 mA.

**Steady-state photoluminescence measurements.** The PL peaks of the cation exchanged films were characterized using a PTI QuantaMaster 400 spectrofluorometer with a xenon arc lamp at an excitation wavelength of 480 nm. A 500 nm shortpass filter was used for the excitation, and a 650 nm longpass filter was used for the emission. The PL peak of  $\text{Al}_2\text{O}_3$  on glass was subtracted from the PL peaks of the cation exchanged films.

**Light sources for time resolved photoluminescence and transient absorption measurements.** The primary light source was a commercial femtosecond Ti:Sapphire regenerative amplifier with a repetition rate of 250 kHz, generating  $\sim 50$  fs (FWHM) pulses centered at 800 nm. The major portion (70 %) of the amplifier output was used to pump an optical parametric amplifier (OPA) to produce excitation pulses centered at 500 nm. A dual prism compressor consisting of two SF10 prisms was used to compensate for group velocity dispersion in the excitation beam. For the transient absorption measurements, a minor portion of the amplifier output (30 %) was focused

onto a sapphire window (10SW8-180, Newport) with 2 mm thickness to generate a single-filament white-light continuum. A pulse near the band edge of the perovskite was selected by using a 10 nm (FWHM) bandpass filter centered at 780 nm (FL780-10, Thorlabs).

**Time-resolved photoluminescence measurements.** Time resolved photoluminescence was performed using a picosecond time-correlated single-photon-counting (TCSPC) technique using an excitation wavelength of 500 nm and intensity of  $0.05 \mu\text{W}/\text{cm}^2$ . The detection system uses the same actively quenched single photon avalanche photodiode (PDM 50CT module, Micro Photon Devices) and a TCSPC module (PicoHarp 300, PicoQuant). The instrument response function (IRF) showed a FWHM of  $\sim 44$  ps as recorded at selected emission wavelengths using a dilute water suspension of coffee creamer. A 40.0-ps channel time was chosen in order to resolve possible fast dynamical processes. A first order decay model (see Equation 1 in the main text) was used to fit the data by minimizing the Chi-squared statistic. In this model, the calculated PL was set equal to the carrier concentration squared. As the time scales relevant for this fitting are significantly longer than the IRF, the calculated PL signal was not convoluted with the IRF.

**Transient absorption measurements.** A 500 nm pulse was used as the probe, and a 780 nm pulse as the probe. The pump and probe beams were overlapped on the sample in such a way that the probe was directed towards a Si photodiode (Nirvana Balanced Photodetector, Newport) after passing through the sample, and the pump was terminated with a beam stop. The signal from the detector was sent to a lock-in amplifier (SR810 DSP, Stanford Research Systems), with a 50  $\mu\text{V}$  typical sensitivity, a 30 ms time constant, and a 24 dB/octave roll off filter. The lock-in amplifier signal data was read out using a data-acquisition module (DAQ, National Instruments Ni PXIe-6124 installed in a NI PXIe-1073 chassis). The delay between the pump and probe beams was set using a DC-motor driven optical delay stage with 0.3 fs resolution (UTS150CC, Newport).

The data was fitted in to the model shown in the main text by minimizing the Chi-squared statistic between the calculated and measured carrier concentrations using MATLAB. This fit was performed globally for the data acquired at pump powers of 0.1, 0.5, 1, and 2mW. The initial carrier profile was estimated from the absorption coefficient at 500 nm.

**Trap-filled limit voltage measurements.** To measure the trap state density through trap-filled limit voltage characterization, pre-patterned indium tin oxide (ITO) coated glass was cleaned using the method detailed in the thin film preparation section. The perovskite layer synthesis and cation exchange were also conducted as detailed in the thin film preparation section. For the top contacts, 500 nm of Au was evaporated onto the films under ultra-high vacuum ( $< 10^{-5}$  torr).

The trap-filled limit voltage was characterized using a Keithley digital multimeter in a nitrogen filled glovebox with PV Measurements I-V software. The voltage range applied spanned from 0 V to 5 V, with 100 I-V points collected. The meter integration was held at 100 PLC with a voltage settling times of 10 ms. The I-V curves were fit with power law equations in both the ohmic and trap-filled limit regimes, with the intersection of these two regimes being the trap-filled limit voltage.

## References

- (1) Kojima, A.; Teshima, K.; Shirai, Y.; Miyasaka, T.; Organometal Halide Perovskites as Visible-Light Sensitizers for Photovoltaic Cells. *J. Am. Chem. Soc.* **2009**, 131, 6050–6051.
- (2) Chen, T.; Chen, W.; Foley, B. J.; Lee, J.; Ruff, J. P. C.; Ko, J. Y. P.; Brown, C. M.; Harriger, L. W.; Zhang, D.; Park, C.; Yoon, M.; Chang, Y.; Choi, J. J.; Lee, S.; Origin of long lifetime of band-edge charge carriers in organic–inorganic lead iodide perovskites. *PNAS*. **2017**, 114, 7519–7524.
- (3) Chen, T.; Foley, B. J.; Ipek, B.; Tyagi, M.; Copley, J. R. D.; Brown, C. M.; Choi, J. J.; Lee, S.; Rotational dynamics of organic cations in the  $\text{CH}_3\text{NH}_3\text{PbI}_3$  perovskite. *Phys. Chem. Chem. Phys.* **2015**, 17, 31278–31286.
- (4) Zhu, X.-Y.; Podzorov, V.; Charge Carriers in Hybrid Organic–Inorganic Lead Halide Perovskites Might Be Protected as Large Polarons. *J. Phys. Chem. Lett.* **2015**, 23, 4758–4761.
- (5) Ma, J.; Wang, L.-W.; Nanoscale Charge Localization Induced by Random Orientations of Organic Molecules in Hybrid Perovskite  $\text{CH}_3\text{NH}_3\text{PbI}_3$ . *Nano Lett.* **2015**, 15, 248–253.
- (6) Stranks, S. D.; Eperon, G. E.; Grancini, G.; Menelaou, C.; Alcocer, M. J.; Leijtens, T.; Herz, L. M.; Petrozza, A.; Snaith, H. J.; Electron-Hole Diffusion Lengths Exceeding 1 Micrometer in an Organometal Trihalide Perovskite Absorber. *Science*. **2013**, 342, 341–344.
- (7) Tan, H.; Che, F.; Wei, M.; Zhao, Y.; Saidaminov, M. I.; Todorović, P.; Broberg, D.; Walters, G.; Tan, F.; Zhuang, T.; Sun, B.; Liang, Z.; Yuan, H.; Fron, H.; Kim, J.; Yang, Z.; Voznyy, O.; Asta, M.; Sargent, E. H.; Dipolar cations confer defect tolerance in wide-bandgap metal halide perovskites. *Nat. Commun.* **2018**, 9, 3100.
- (8) Miyata, K.; Meggiolaro, D.; Tuan Trinh, M.; Joshi, P. P.; Mosconi, E.; Jones, S. C.; De Angelis, F.; Zhu, X.-Y.; Large polarons in lead halide perovskites. *Sci. Adv.* **2017**, 3, 1701217.
- (9) Miyata, K.; Atallah, T. L.; Zhu, X.-Y.; Lead halide perovskites: Crystal-liquid duality, phonon glass electron crystals, and large polaron formation. *Sci. Adv.* **2017**, 3, 1701469.
- (10) Nagai, M.; Tomioka, T.; Ashida, T.; Hoyano, M.; Akashi, R.; Yamada, Y.; Aharen, T.; Kanemitsu, Y.; Longitudinal Optical Phonons Modified by Organic Molecular Cation Motions in Organic-Inorganic Hybrid Perovskites. *Phys. Rev. Lett.*, **2018**, 121, 145506.
- (11) Etienne, T.; Mosconi, E.; De Angelis, F.; Dynamical Origin of the Rashba Effect in Organohalide Lead Perovskites: A Key to Suppressed Carrier Recombination in Perovskite Solar Cells? *J. Phys. Chem. Lett.* **2016**, 7, 1638–1645.
- (12) Zheng, F.; Tan, L. Z.; Liu, S.; Rappe, A. M.; Rashba Spin–Orbit Coupling Enhanced Carrier Lifetime in  $\text{CH}_3\text{NH}_3\text{PbI}_3$ . *Nano Lett.* **2015**, 15, 7794–7800.
- (13) Park, M.; Neukirch, A. J.; Reyes-Lillo, S. E.; Lai, M.; Ellis, S. R.; Dietze, D.; Neaton, J. B.; Yang, P.; Tretiak, S.; Mathies, R. A.; Excited-state vibrational dynamics toward the polaron in methylammonium lead iodide perovskite. *Nat. Commun.* **2018**, 9, 2525.
- (14) Cinquanta, E.; Meggiolaro, D.; Motti, S. G.; Gandini, M.; Alcocer, M. J. P.; Akkerman, Q. A.; Vozzi, C.; Manna, L.; De Angelis, F.; Petrozza, A.; Stagira, S.;

Ultrafast THz Probe of Photoinduced Polarons in Lead-Halide Perovskites. *Phys. Rev. Lett.*, **2019**, 122, 166601.

- (15) Frohna, K.; Deshpande, T.; Harter, J.; Peng, W.; Barker, B. A.; Neaton, J. B.; Louie, S. G.; Bakr, O. S.; Hsieh, D.; Bernardi, M.; Inversion symmetry and bulk Rashba effect in methylammonium lead iodide perovskite single crystals. *Nat. Commun.* **2018**, 9, 1829.
- (16) Filippetti, A.; Mattoni, A.; Hybrid perovskites for photovoltaics: Insights from first principles. *Phys. Rev. B.* **2014**, 89, 125203.
- (17) Mateen, M.; Arain, Z.; Liu, C.; Yang, Y.; Liu, X.; Ding, Y.; Shi, P.; Ren, Y.; Wu, Y.; Dai, S.; Hayat, X.; Alsaedi, A.; High-Quality (FA)<sub>x</sub>(MA)<sub>1-x</sub>PbI<sub>3</sub> for Efficient Perovskite Solar Cells via a Facile Cation-Intermixing Technique. *ACS Sustainable Chem. Eng.* **2019**, 7, 11760-11768.
- (18) Conings, B.; Babayigit, A.; Klug, M. T.; Bai, S.; Gauquelin, N.; Sakai, N.; Wang, J. T.; Verbeeck, J.; Boyen, H.; Snaith, H. J.; A Universal Deposition Protocol for Planar Heterojunction Solar Cells with High Efficiency Based on Hybrid Lead Halide Perovskite Families. *Adv. Mater.* **2016**, 28, 10701–10709.
- (19) Jeon, N. J.; Noh, J. H.; Yang, W. S.; Kim, Y. C.; Ryu, S.; Seo, J.; Seok, S. I.; Compositional engineering of perovskite materials for high-performance solar cells. *Nature.* **2015**, 517, 476–480.
- (20) Jesper Jacobsson, T.; Correa-Baena, J. P.; Pazoki, M.; Saliba, M.; Schenk, K.; Gratzel, M.; Hagfeldt, A.; Exploration of the compositional space for mixed lead halogen perovskites for high efficiency solar cells. *Energy & Environ. Sci.* **2016**, 9, 1706–1724.
- (21) Shi, D. et al. Low trap-state density and long carrier diffusion in organolead trihalide perovskite single crystals. *Science*, **2015**, 347, 519–522.
- (22) Gu, X. et al. Enhanced electronic transport in Fe 3+ -doped TiO<sub>2</sub> for high efficiency perovskite solar cells. *J. Mater. Chem. C.* **2017**, 5, 10754–10760.
- (23) Jain, A.; Kumar, P.; Jain, S. C.; Kumar, V.; Mehra, R. M.; Trap filled limit voltage (VTFL) and V<sub>2</sub> law in space charge limited currents. *J. Appl. Phys.* **2007**, 102, 094505.
- (24) Wehrenfennig, C.; Eperon, G. E.; Johnston, M. B.; Snaith, H. J.; Herz, L. M.; High charge carrier mobilities and lifetimes in organolead trihalide perovskites. *Adv. Mater.* **2014**, 26, 1584–1589.
- (25) Johnston, M. B.; Herz, L. M.; Hybrid Perovskites for Photovoltaics: Charge-Carrier Recombination, Diffusion, and Radiative Efficiencies. *Acc. Chem. Res.* **2016**, 49.
- (26) Simpson, M. J.; Doughty, B.; Yang, B.; Xiao, K.; Ma, Y.-Z.; Imaging Electronic Trap States in Perovskite Thin Films with Combined Fluorescence and Femtosecond Transient Absorption Microscopy. *J. Phys. Chem. Lett.* **2016**, 7, 1725–1731.
- (27) Shockley, W.; Read, W. T.; Statistics of the Recombinations of Holes and Electrons. *Phys. Rev.* **1952**, 87, 835–842.
- (28) Stranks, S. D.; Burlakov, V. M.; Leijtens, T.; Ball, J. M.; Goriely, A.; Snaith, H. J.; Recombination Kinetics in Organic-Inorganic Perovskites: Excitons, Free Charge, and Subgap States. *Phys. Rev. Applied.* **2014**, 2, 034007.

- (29) Hutter, E. M.; Eperon, G. E.; Stranks, S. D.; Savenije, T. J.; Charge Carriers in Planar and Meso-Structured Organic–Inorganic Perovskites: Mobilities, Lifetimes, and Concentrations of Trap States. *J. Phys. Chem. Lett.* **2015**, *6*, 3082–3090.
- (30) Yamada, Y.; Nakamura, T.; Endo, M.; Wakamiya, A.; Kanemitsu, Y.; Photocarrier Recombination Dynamics in Perovskite  $\text{CH}_3\text{NH}_3\text{PbI}_3$  for Solar Cell Applications. *J. Am. Chem. Soc.* **2014**, *136*, 11610–11613.
- (31) Draguta, S.; Thakur, S.; Morozov, Y. V.; Wang, Y.; Manser, J. S.; Kamat, P. V., Kuno, M.; Spatially Non-uniform Trap State Densities in Solution-Processed Hybrid Perovskite Thin Films. *J. Phys. Chem. Lett.* **2016**, *7*, 715–721.
- (32) Bretschneider, S. A.; Ivanov, I.; Wang, H. I.; Miyata, K.; Zhu, X.; Bonn, M.; Quantifying Polaron Formation and Charge Carrier Cooling in Lead-Iodide Perovskites. *Adv. Mater.* **2018**, *30*, 1707312.
- (33) Tan, H.; Che, F.; Wei, M.; Zhao, Y.; Saidaminov, M. I.; Supplementary Information for Dipolar cations confer defect tolerance in wide-bandgap metal halide perovskites. *Nat. Commun.* **2018**, *9*, 3100.
- (34) Foley, B. J.; Cuthriell, S.; Yazdi, S.; Chen, A. Z.; Guthrie, S. M.; Deng, X.; Giri, G.; Lee, S.-H.; Xiao, K.; Doughty, B.; Ma Y.-Z.; Choi, J. J.; *Nano Lett.* **2018**, *18*, 6271-6278.
- (35) Simpson, M. J.; Doughty, B.; Yang, B.; Xiao, K.; Ma, Y. -Z.; *ACS Photonics*, **2016**, *3*, 434-442.
- (36) Simpson, M. J.; Doughty, B.; Yang, B.; Xiao, K.; Ma, Y. -Z.; *J Phys Chem Lett*, **2015**, *6*, 3041-3047.
- (37) Simpson, M. J.; Doughty, B.; Yang, B.; Xiao, K.; Ma, Y. -Z.; *J Phys Chem Lett*, **2017**, *8*, 3299-3305.
- (38) Dastidar, S.; Li, S.; Smolin, S. Y.; Baxter, J. B.; Fafarman, A. T.; Slow Electron–Hole Recombination in Lead Iodide Perovskites Does Not Require a Molecular Dipole. *ACS Energy Lett.* **2017**, *2*, 2239–2244.
- (39) Motta, C.; El-Mellouhi, F.; Kais, S.; Tabet, N.; Alharbi, F.; Sanvito, S.; Revealing the role of organic cations in hybrid halide perovskite  $\text{CH}_3\text{NH}_3\text{PbI}_3$ . *Nat. Commun.* **2015**, *6*, 7026.
- (40) Xie, L.-Q.; Chen, L.; Nan, Z.-A.; Lin, H.-X.; Wang, T.; Zhan, D.-P.; Yan, J.-W.; Mao, B.-W.; Tian, Z.-Q.; Understanding the Cubic Phase Stabilization and Crystallization Kinetics in Mixed Cations and Halides Perovskite Single Crystals. *J. Am. Chem. Soc.* **2017**, *139*, 3320-3323.
- (41) Saliba, M.; Matsui, T.; Domanski, K.; Seo, J. -Y.; Ummadisingu, A.; Zakeeruddin, S. M.; Correa-Baena, J. -P.; Tress, W. R.; Abate, A.; Hagfeldt, A.; Grätzel, M.; Incorporation of rubidium cations into perovskite solar cells improves photovoltaic performance. *Science*. **2016**, *354*, 206-209.
- (42) Dai, J.; Fu, Y.; Manger, L. H.; Rea, M. T.; Hwang, L.; Goldsmith, R. H.; Jin, S.; Carrier Decay Properties of Mixed Cation Formamidinium–Methylammonium Lead Iodide Perovskite  $[\text{HC}(\text{NH}_2)_2]_{1-x}[\text{CH}_3\text{NH}_3]_x\text{PbI}_3$  Nanorods. *J. Phys. Chem. Lett.* **2016**, *7*, 5036-5043.

- (43) Liu, J.; Shirai, Y.; Yang, X.; Yue, Y.; Chen, W.; Wu, Y.; Islam, A.; Han, L.; High-Quality Mixed-Organic-Cation Perovskites from a Phase-Pure Non-stoichiometric Intermediate  $(\text{FAI})_{1-x}\text{PbI}_2$  for Solar Cells. *Adv. Mater.* **2015**, 27, 4918-4923.
- (44) Salado, M.; Calio, L.; Berger, R.; Kazim, S.; Ahmad, S.; Influence of the mixed organic cation ratio in lead iodide based perovskite on the performance of solar cells. *Phys. Chem. Chem. Phys.* **2016**, 18, 27148-27157.
- (45) Huang, Y. et al. The intrinsic properties of  $\text{FA}_{(1-x)}\text{MA}_x\text{PbI}_3$  perovskite single crystals. *J. Mater. Chem. A.* **2017**, 5, 8537-8544.
- (46) Chen, J.; Xu, J.; Xiao, L.; Zhang, B.; Dai, S.; Yao, J.; Mixed-Organic-Cation  $(\text{FA})_x(\text{MA})_{1-x}\text{PbI}_3$  Planar Perovskite Solar Cells with 16.48% Efficiency via a Low-Pressure Vapor-Assisted Solution Process. *ACS Appl. Mater. Interfaces.* **2017**, 3, 2449-2458.